Volume 3 | Number 5 | May 2019

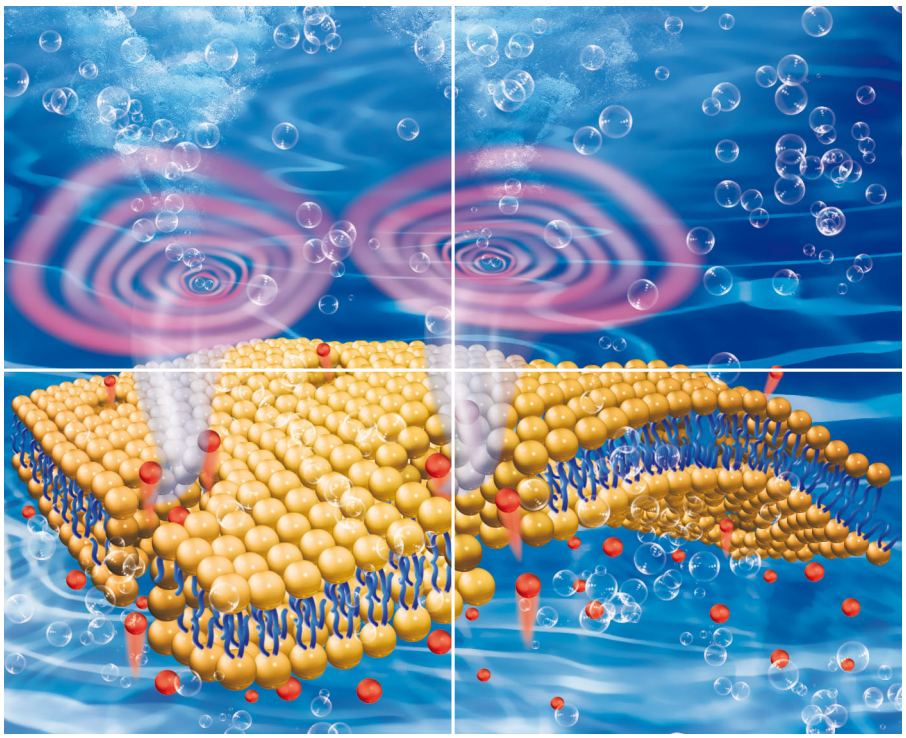

MATERIALS CHEMISTRY

FRONTIERS

CCS 中国化学会 CHINESE CHEMICAL SOCIETY
ICCAS 1956
ROYAL SOCIETY OF CHEMISTRY | Celebrating IYPT 2019
rsc.li/frontiers-materials

MATERIALS CHEMISTRY
FRONTIERS

RESEARCH ARTICLE

View Article Online
View Journal | View Issue

Cite this: *Mater. Chem. Front.*, 2019, **3**, 782

Received 16th November 2018,
Accepted 9th January 2019

DOI: 10.1039/c8qm00589c

rsc.li/frontiers-materials

Hypersonic poration of supported lipid bilayers†

Yao Lu,[ab] Jurriaan Huskens,*[b] Wei Pang[a] and Xuexin Duan*[a]

Hypersound (ultrasound of gigahertz (GHz) frequency) has been recently introduced as a new type of membrane-disruption method for cells, vesicles and supported lipid bilayers (SLBs), with the potential to improve the efficiency of drug and gene delivery for biomedical applications. Here, we fabricated an integrated microchip, composed of a nano-electromechanical system (NEMS) resonator and a gold electrode as the extended gate of a field effect transistor (EGFET), to study the effects of hypersonic poration on an SLB in real time. The current recordings revealed that hypersound enabled ion conduction through the SLB by inducing transient nanopores in the membrane, which act as the equivalent of ion channels and show gating behavior. The mechanism of pore formation was studied by cyclic voltammetry (CV), atomic force microscopy (AFM) and laser scanning microscopy (LSM), which support the causality between hypersound-triggered deformation and the reversible membrane disruption of the SLB. This finding contributes to the development of an approach to reversibly control membrane permeability by hypersound.

Introduction

Physical methods based on the principle of membrane disruption, such as thermal poration,[1–3] optoporation,[4–6] electroporation[7–9] and sonoporation,[10–12] have been widely adopted to improve the efficiency of intracellular delivery. The key to the enhanced uptake of extracellular substances lies in their physical interaction with the cells, which can improve the permeability of the cell membrane without any further damage to assist the entry of foreign molecules. Among these techniques, sonoporation induced by ultrasound has gained much attention in various drug delivery and therapeutic applications.[13–16]

In a conventional sonoporation process, the most significant effect of ultrasound involves the nucleation, growth and oscillation of microbubbles, a phenomenon referred to as cavitation.[17–19] Cavitation includes either the rapid collapse of microbubbles (inertial cavitation) or the sustained oscillatory motion of microbubbles (stable cavitation), both of which can induce strong mechanical effects on the cell membrane.[20–22] The collapse of microbubbles generates shock waves with an extensive amplitude that disturbs the cell membrane, whereas the stable oscillation of microbubbles can induce acoustic pressure in the liquid and exert shear stress on the membrane.[23–25] The degree of membrane permeability upon sonoporation mainly depends on the frequency and duration of the applied ultrasound.[26–28] Since ultrasound spans a frequency of roughly 15 kHz to 10 MHz in liquid, with an associated acoustic wavelength of 10 to 0.01 cm, no direct coupling of the acoustic field with the cell membrane can be detected at a molecular level,[29] which restricts the direct formation of pores at the cell membrane and creates a strong dependence on microbubble agents.[30,31]

In principle, the increase of the ultrasonic frequency will accelerate the oscillation of cavitation bubbles as well as enhance the acoustic pressure.[32,33] Thus, an acoustic wave of gigahertz (GHz) frequency and (sub)micrometer wavelength, which is defined as hypersound,[34,35] has been proposed to affect membrane permeability.[36] It has been reported that hypersound can be applied to enhance the delivery of drug molecules into cancer cells by creating transient nanopores in the cell membrane, which showed no cytotoxicity.[37] The mechanical stress on the membrane surface is significantly enhanced by hypersonic poration compared with the conventional ultrasonic treatment. Furthermore, hypersound has also been applied in a layer-by-layer (LbL) system to control the disassembly of supramolecular membrane structures.[38] Despite the strong potential of hypersound in both drug delivery and controlled release, the mechanism of hypersonic poration is still not fully understood.

In this work, hypersonic poration was studied by analyzing the acoustic behavior of a supported lipid bilayer (SLB). A high-frequency nanofabricated resonator of 1.6 GHz was used to generate hypersound with a submicron wavelength. On the same microchip, a gold electrode has been integrated and

[a] *State Key Laboratory of Precision Measuring Technology & Instruments, Tianjin University, Tianjin 300072, China. E-mail: xduan@tju.edu.cn*
[b] *Molecular Nanofabrication Group, MESA+ Institute for Nanotechnology, University of Twente, 7500 AE, Enschede, The Netherlands. E-mail: j.huskens@utwente.nl*

† Electronic supplementary information (ESI) available: Microfabrication process of the integrated microchip, fluorescence characterization of the supported lipid bilayer and theoretical simulations results of hypersound induced deformation of the lipid membrane. Simultaneous fluorescence imaging and electrical detection of membrane conductance by applying hypersound of 30 mW (Video S1), 50 mW (Video S2) and 250 mW (Video S3). See DOI: 10.1039/c8qm00589c

connected with an extended gate electrode of a field effect transistor (EGFET)[39,40] to monitor the currents through the SLB induced by hypersound. The ion-channel effects of hypersonic poration were measured and analyzed with salt solutions containing cations with different valences. Characterization by cyclic voltammetry (CV), atomic force microscopy (AFM), and laser scanning microscopy (LSM) was performed to feature the properties of hypersonic nanopores. This study thus aims to provide a better understanding of the mechanism of hypersonic poration and to create an approach capable of changing and monitoring membrane permeability in real time.

Experimental section

Materials

All chemicals including phosphate-buffered saline (PBS), potassium chloride (KCl), calcium chloride ($CaCl_2$), iron(III) chloride ($FeCl_3$) and potassium ferricyanide ($K_3Fe(CN)_6$) were purchased from Sigma Aldrich. PBS was dissolved in ultrapure water to obtain the 0.1 M buffer solution (including 0.1 M sodium dihydrogen phosphate and 0.15 M sodium chloride, pH 7.4). The metal ion chlorides were dissolved in pure water to obtain 2 mM electrolyte solutions. $K_3Fe(CN)_6$ was dissolved in 1 M KCl solution to obtain a 1 mM solution for the cyclic voltammetry tests.

Fabrication of the supported lipid bilayer

The lipid 1-palmitoyl-2-oleoyl-*sn-glycero*-3-phospho-1′-glycerol (POPG) was purchased from AVANTI and dissolved in chloroform with a typical concentration of 0.5 mg mL^{-1}. The supported lipid bilayer (SLB) was fabricated and coated on the integrated chip by the Langmuir–Blodgett (LB) method[41,42] using a Langmuir trough (Kibron, MicroTrough XL). In brief, 50 μL of the POPG solution was spread onto the surface of pre-cleaned Milli-Q water and then compressed at a speed of 10 mm min^{-1} until the targeted surface pressure of 25 mN m^{-1} was reached. Afterwards, the integrated chip, which was previously oxidized in air plasma for 5 min to create a hydrophilic interface, was vertically pulled up from the water subphase at a constant speed of 1 mm min^{-1} to form a single lipid layer and then down into the LB trough again to form the SLB.

Membrane characterization

The SLB coating on the integrated chip was characterized by cyclic voltammetry (CV, CHI 660E, Huachen), fluorescence microscopy (Olympus IXplore Pro), atomic force microscopy (AFM, Veeco, Nano Scope III) in tapping mode and laser scanning microscopy (LSM, Olympus LEXT OLS4000).

Fabrication of the integrated microchip

The integrated device was fabricated according to a previously published process (see ESI,† Fig. S1).[43] Before the fabrication of the resonator, a Bragg reflector was mounted on the silicon wafer by alternately depositing three pairs of silicon dioxide (SiO_2) and molybdenum (Mo) thin films.[44] The first layer of the Bragg reflector was used as the bottom electrode followed by the sputtering of highly *c*-axis oriented aluminum nitride (AlN) film as a piezoelectric layer and another layer of Mo as the top electrode.[45] Finally, 300 nm Au was deposited and employed as the extended gate electrode of a field effect transistor (EGFET).

Real-time detection system

The integrated chip was mounted onto a two-channel evaluation board with the wire bonding technique.[46] Sinusoidal signals of 1.6 GHz were generated by a signal generator (Agilent, N5181A), amplified by a power amplifier (Mini-Circuits, ZHL-5W-422), and sent to the nano-electromechanical system (NEMS) resonator, which then transduced the electrical supply to mechanical vibrations and generated hypersound. The gold electrode was connected to a commercially available back-end field effect transistor (FET, ALD110800A, Advanced Linear Devices). The back-end transistor was an *n*-channel FET with a zero-volt threshold voltage necessary to avoid the destruction of lipid membranes at any positive or negative voltage. A miniature Ag/AgCl reference electrode (World Precision Instruments, Inc.) was used to bias the transistor to the desired working point. FET characteristics was confirmed off-line using a Keithley 2400 Source Measure Unit (SMU) before real-time measurement at a constant bias voltage of 0.3 V to ensure the FET working in the linearly amplified zone.

Results and discussion

Working principle

The microchip integrated with an acoustic nano-electromechanical system (NEMS) resonator and a gold electrode is shown in Fig. 1a. The polygonal shape of the NEMS resonator was designed to enhance its main-mode vibration while minimizing the parasitic effect.[37] By coupling the vertical electric field through a specific piezoelectric coefficient, the resonator vibrates in a longitudinal mode and generates hypersound of gigahertz (GHz) frequency.[47] A quarter-wavelength Bragg reflector was placed under the resonance structure to avoid the dissipation of energy into the silicon substrate.[48]

The working principle of this integrated microchip is illustrated in Fig. 1b. An artificial supported lipid bilayer (SLB) made of 1-palmitoyl-2-oleoyl-*sn-glycero*-3-phospho-1′-glycerol (POPG) was deposited on the surface of the microchip, covering both the resonator and the gold electrode. POPG was used as the component of the SLB to mimic the negatively charged nature of cell membranes and because it shows good flexibility at room temperature which facilitates membrane deformation and poration. Once activated, the vibrating interface of the resonator drives the motion of the SLB deposited on top of the resonator and induces a propagation of hypersound within the lipid membrane, from the vibrated area of the resonator to the gold electrode. The embedded gold electrode was connected with the gate electrode of a back-end field effect transistor (FET) and was used as the charge-sensitive interface for current measurements.[43] Since an SLB is highly resistive and impermeable to hydrated ions,[49] the electrical potential of the underlying gold electrode can remain constant in a pure electrolyte solution by the isolation from the intact SLB. However, when hypersound

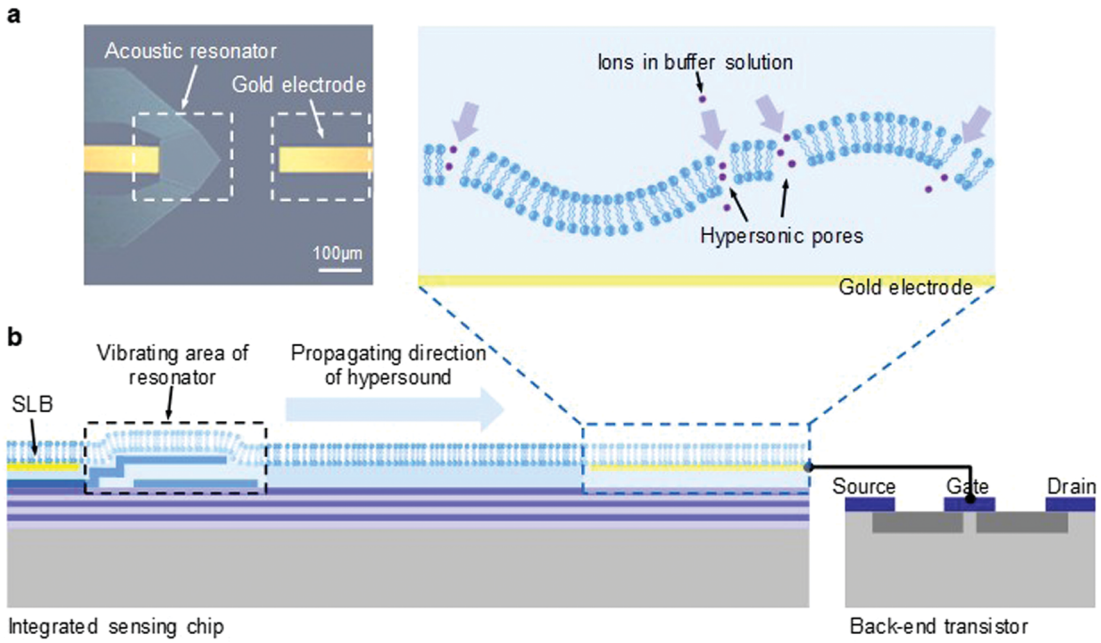

Fig. 1 A microfabricated chip integrating a high-frequency NEMS resonator (1.6 GHz) with a gold electrode. (a) Top view of the polygon-shaped resonator and the integrated gold electrode in the same chip. (b) Schematic illustration of the integrated sensing system. The SLB is coated on the surface of the microchip, covering both the resonator and the gold electrode. The gold electrode is connected with the gate electrode of the FET (referred to as an extended-gate FET, EGFET) and is used as the front-end sensing electrode for electrical measurements. The zoom-in image shows that some pore-like membrane defects occur during the deformation of the SLB induced by the propagation of hypersound. Consequently, ions from the buffer solution can be translocated across the membrane and cause potential changes of the gold electrode.

is applied, the transduction of the motion of the resonator to and through the SLB may deform the membrane structure. Once membrane defects occur during this process (as shown in the zoom-in image), the SLB becomes permeable to ions, thus inducing membrane conductivity that can be detected by electrical measurements from the back-end FET.

Characterization of the supported lipid bilayer

Fig. 2a shows the surface pressure–area (π–A) compression isotherm of POPG. The target surface pressure for the formation of SLB was fixed at 25 mN m^{-1} to ensure the compactness of the membrane. Cyclic voltammetry (CV) tests were conducted using $K_3Fe(CN)_6$ as a redox probe to confirm the integrity of the artificial SLB. As shown in Fig. 2b, the formation of the SLB on the gold electrode significantly reduced the measured faradaic current compared with the uncovered electrode, suggesting that an insulating SLB was successfully placed on top of the device with the LB method.

Real-time detection of hypersonic poration

The real-time electrical response of the SLB was recorded by periodically switching on and off the stimulation of hypersound.

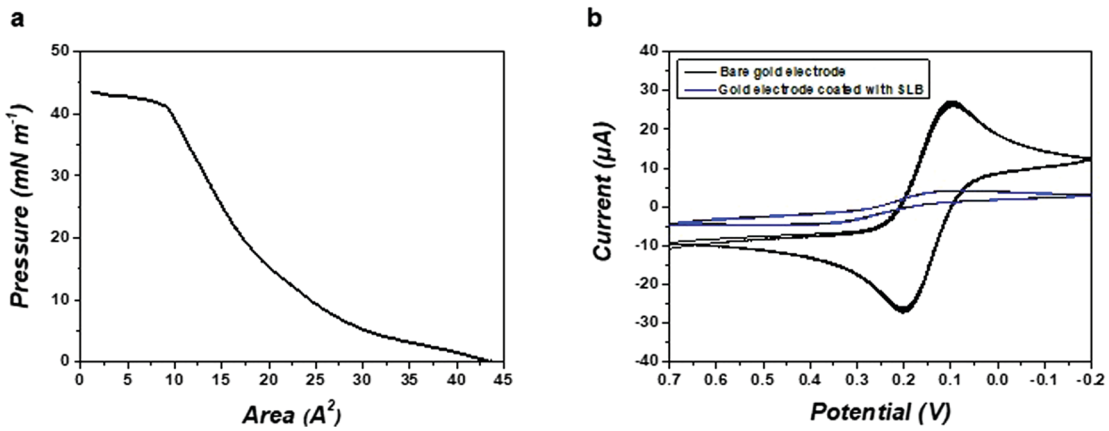

Fig. 2 Characterization of the SLB assembled on the integrated microchip. (a) π–A compression isotherm of POPG at the air–water interface at room temperature. (b) CV responses of 1 mM $K_3Fe(CN)_6$ in 1 M KCl at the embedded gold electrode of the integrated microchip (black: bare electrode without SLB, blue: electrode coated with the SLB).

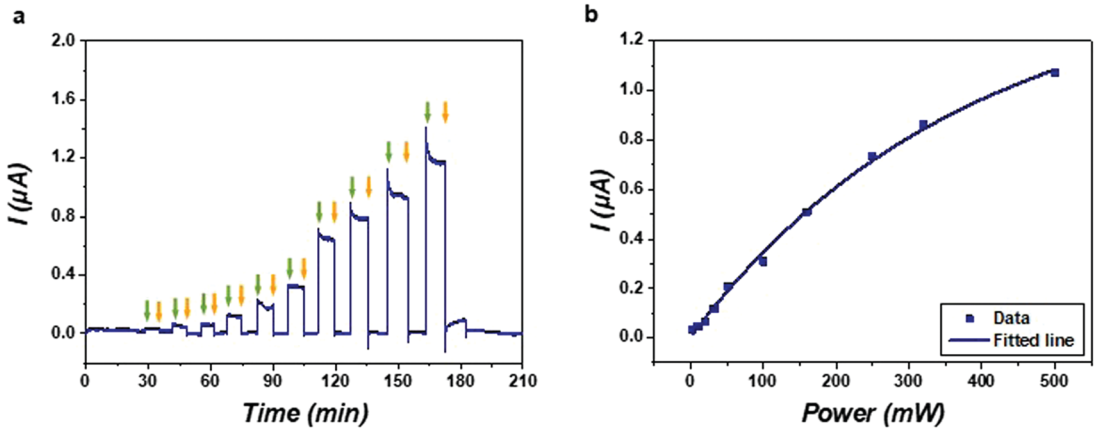

Fig. 3 (a) Real-time detection of ion current through the SLB on the integrated device by alternatingly switching on (green arrows) and off (orange arrows) the hypersound (the input powers were successively 3.2, 10, 20, 32, 50, 100, 160, 250, 320 and 500 mW). The buffer solution was PBS (0.1 M, pH 7.4). (b) Data points (markers) and exponential fitting (line) of the ion current as a function of input power. Here, the exponential fitting was applied to show the current trend without any physical meanings.

As shown in Fig. 3a, the current curve exhibited an instantaneous increase when turning on the hypersound and maintained a constant value during sustained stimulation (see also Videos S1–S3 in ESI†), indicating that the applied hypersound caused conductivity through the SLB, ascribed to induced permeability to the ions present in the buffer solution. The current curve recovered readily to its original value upon switching off the hypersound, indicating the reversibility of the induced membrane permeability. As the patterns of the SLBs in Videos S1–S3 (ESI†) show, it is likely that the lipid membrane coated on the microchip was mechanically disrupted by deforming the SLB through the propagation of hypersound. In this acoustical disruption process that occurs by coupling with the acoustic waves at a sub-micron length scale, some transient nanopores are generated to allow for the ion transfer across the SLB. Since hypersound can form strong turbulent flow inside fluids,[50] the ion transfer can also be facilitated by the accompanying acoustic streaming effects. Due to the flexibility of the lipid membrane and the molecular diffusion of the lipid molecules therein, the membrane defects can then be healed in a re-assembly process by turning off the hypersound. Interestingly, the transmembrane current induced by hypersound resembles the stochastic "gating" behavior of biological ion channels.[51] Instead of modulating the ion-channel currents with reversibly binding blocker molecules, the current through the SLB can be mediated by the formation and closure of the transient pores formed by hypersound.

Subsequently, the ion current was modulated with hypersound of different input powers as shown in the current–time trace (Fig. 3a). The first step of the ion current was in response to hypersound of 3.2 mW; thereafter the current values increased step by step with the increase of input power. It is likely that more and/or longer lasting transient nanopores were generated with hypersound of higher power, and this high acoustic intensity also enhanced the ion transfer by accelerating the velocity of acoustic streaming.[50] The magnitude of the current through the transient pores was plotted as a function of input power, which shows a response to hypersound that levels off at high powers (Fig. 3b). In the low power range (less than 250 mW), the current almost increased linearly with the input power, while at higher input power, the current increased much more slowly and presented a trend of saturation, which is likely due to limitation of the number of hypersonic pores within the restricted area of the SLB. In the absence of an SLB, a significantly higher current was observed (Fig. S5, ESI†), and changing the KCl concentration from 2–100 mM in the presence of an SLB showed little variation of the hypersound-induced current (Fig. S6, ESI†). These results support that the limited formation of hypersonic pores is the main factor for the current saturation observed in Fig. 3b.

To understand how GHz hypersound was generated and its waves propagated along the surface of the NEMS resonator, a 2D finite element model (FEM) of the single resonator was employed (Fig. S3, ESI†). It shows that the surface of the resonator deformed to generate hypersound, the magnitude of which is around several nanometers. We assume that the nanoscale deformation of the resonator drives the deformation of the SLB coating on its surface. By increasing the input power of hypersound, the surface of the resonator deformed more strongly (illustrated in Table S1, ESI†), which is in accordance with the increased currents in Fig. 3.

To further investigate the mechanism of hypersonic poration, ion currents through the SLB were measured in solutions containing salts with cations of different valences. The current curves probed in solutions of KCl, $CaCl_2$ and $FeCl_3$ of the same concentration (2 mM in pure water) are shown in Fig. 4a. Similar measurements were also performed in solutions of NaCl and $MgCl_2$ (Fig. S7, ESI†), and these results resemble those of KCl and $CaCl_2$, respectively. To ensure the applied hypersound was in the linear range, the value of the input power was limited to 250 mW. All current curves were found to increase with hypersound of higher input powers, and importantly, the currents were different for solutions containing different salts. In Fig. 4b, the fit results of currents generated from solutions containing the different salts all showed a linear trend as a function of input power, which is in accordance with the results presented in Fig. 3b (below 250 mW).

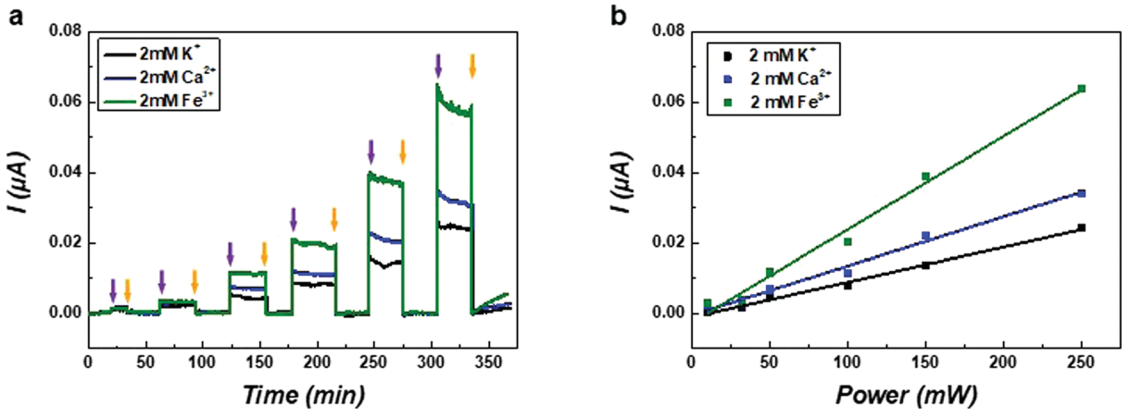

Fig. 4 (a) Real-time recordings of the ion current through the SLB on the integrated device by alternatingly switching on (purple arrows) and off (orange arrows) the hypersound (the input powers were successively 10, 32, 50, 100, 160, 250 mW). The electrolyte solutions were respectively KCl, $CaCl_2$ and $FeCl_3$ (2 mM in pure water). (b) Data points (markers) and linear fits (lines) of the ion current as a function of input power.

These results support therefore that the value of the current through the transient nanopores in the SLB can be quantitatively controlled by adjusting the intensity of hypersound, which can be consequently used to adjust the premeability of the lipid membrane.

The increased current responses for $CaCl_2$ and $FeCl_3$ compared with KCl can possibly be attributed to (i) increased ionic strength, (ii) increased concentration of chloride, and/or (iii) a direct effect of the valence of the cation. Because the negative surface charge of POPG is screened by mobile counterions with positive charge, the overall ionic current through the SLB is mainly induced by the translocation of cations through the pore-like structures.[52] Therefore, the non-linear current trend for different cations can probably be related to a complex and combined effect of ionic strength and specific cation properties regarding their valence and possibly to mobilities affected by acoustic streaming. However, more data would be needed to discriminate between these possibilities.

Characterization of hypersonic poration

To evaluate the formation of hypersonic pores at the lipid membrane, cyclic voltammograms using the ferro/ferricyanide redox couple were recorded with the SLB-coated gold electrode in the presence and absence of hypersound. As shown in Fig. 5a, the redox response increased with switching on the hypersound (500 mW) in real time, indicating a transport of the redox couple to the gold electrode coupled to electron transfer, which was induced by the exposure of the electrode upon pore formation. Once the last CV cycle was ended, another CV cycle was recorded upon switching off the hypersound, and the duration of this hypersonic treatment was less than 1 min. As shown in Fig. 5a, the redox peaks were reduced immediately and overlapped with the CV curve obtained in the absence of hypersound, indicating that the oxidation and reduction of ions was reduced to the base level at the shielded electrode. This data confirms that the hypersound-induced pore formation is fast and reversible, and the integrity of the SLB is restored upon ending the stimulation by hypersound.

The morphology of the SLB was analyzed by atomic force microscopy (AFM) before and after the stimulation by hypersound. All the measurements were conducted in liquid phase using tapping mode. Since the platform of AFM is not compatible with the hypersound setup, it cannot provide real-time information of morphological changes occurring at the SLB during hypersound operation. Therefore, hypersound was applied to the SLB for a prolonged period of time until the transient nanopores transformed into permanent defects, which can then be detected with AFM. The transition from reversible pores to irreversible damage was determined by CV by gradually increasing the duration of hypersound until the redox peaks did not diminish any more after switching off the hypersound (Fig. S4, ESI†). As shown in Fig. 5b, the original surface of the SLB was essentially flat and featureless. Note that the detected height of the lipid bilayer was slightly higher (approx. 10 nm) than the normal value (4–5 nm) obtained from dry lipid membranes, which can be attributed to the effects of liquid in tapping mode.[53] The morphology of the SLB was first detected after a short treatment of hypersound (250 mW, 5 min), where no obvious difference was observed on the membrane surface (Fig. 5c), indicating that hypersound of lower intensity and duration does not damage the structure of the SLB irreversibly. In contrast, when the applied hypersound was increased to 500 mW for 30 min, the morphology of the membrane was changed (Fig. 5d). The average height increased from 13.7 ± 0.6 nm (Fig. 5b) to 16.8 ± 1.0 nm, and clear defects were observable on the membrane surface (Fig. 5d). These results confirm the existence of morphological effects of hypersound on the SLBs.

To assess the structural changes of the membrane, laser scanning microscopy (LSM), which is compatible with the hypersound setup, was used for studying the hypersonic pores at the SLB in a real-time fashion. The duration of hypersound for all the microscopy measurements was less than 1 min during the scanning process. One intact SLB made of POPG was deposited on the integrated device, covering both the NEMS resonator and the embedded gold electrode to guarantee the membrane continuity from the resonator to the gold electrode. The confocal image of Fig. 6a shows the morphology of the section of the SLB

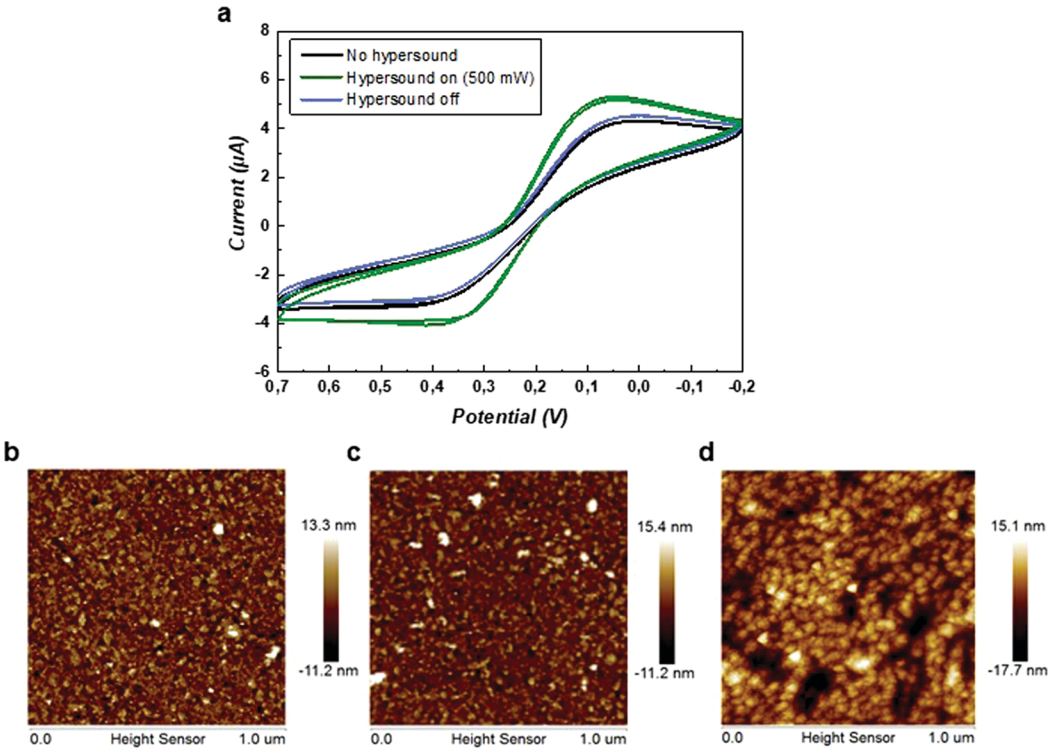

Fig. 5 Characterization of hypersonic poration at a SLB. (a) Real-time CV responses of 1 mM $K_3Fe(CN)_6$ in 1 M KCl at SLB by switching on (500 mW, <1 min) and off the hypersound. The black curve was obtained with the original SLB before any treatment of hypersound. The green curve was obtained by simultaneously switching on the hypersound. After the duration of a CV cycle, hypersound was immediately switched off and another CV cycle (blue) was recorded. (b) AFM images of SLB (b) before any treatment of hypersound. (c) After treated with hypersound of 250 mW for 5 min and (d) then treated with hypersound of 500 mW for 30 min.

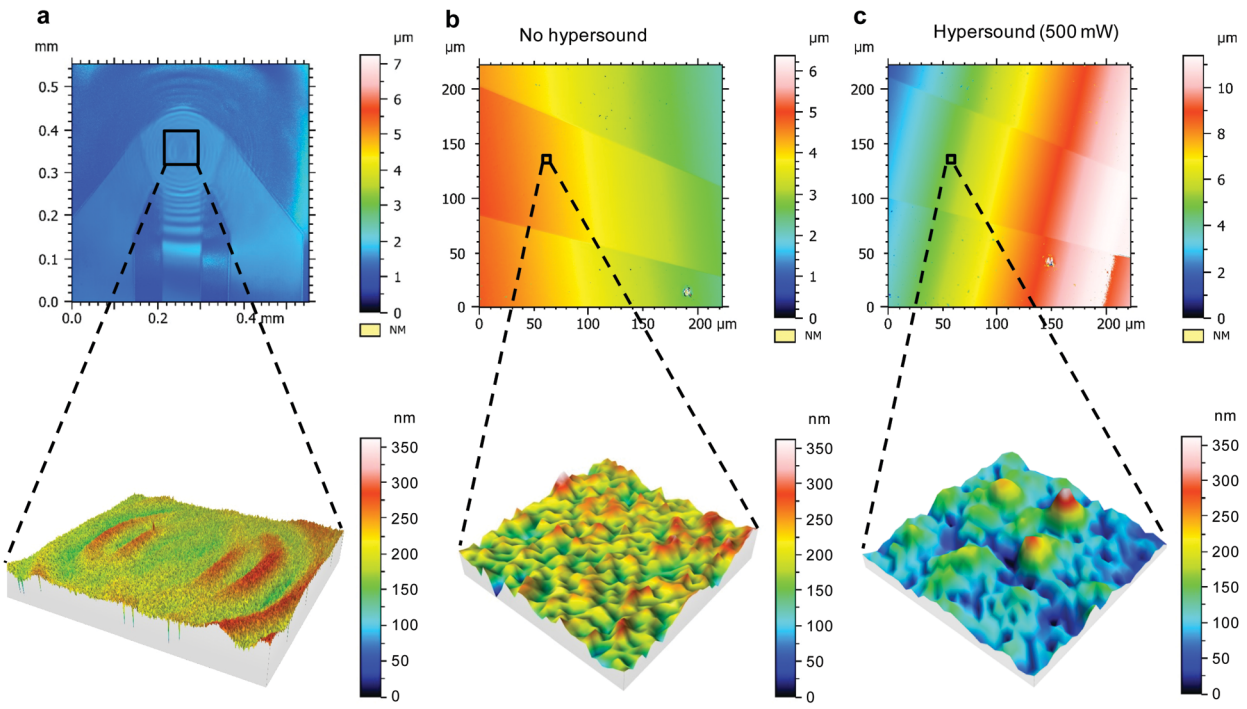

Fig. 6 Real-time LSM images of a SLB made of POPG on the integrated device in the absence or presence of the stimulation by hypersound (500 mW). (a) Morphology of the SLB on top of the activated NEMS resonator (the surface layer is AlN). The sizes of the 2D map and the 3D zoom-in image are respectively 450 × 550 μm^2 and 100 × 100 μm^2. Morphology of SLB on top of the gold electrode before (b) and after (c) the stimulation by hypersound. Hypersound was on only during scan (b), and each scan took <1 min. The sizes of the 2D maps and the 3D zoom-in images are respectively 220 × 220 μm^2 and 2 × 2 μm^2.

coated on top of the activated NEMS resonator. Here, the color and contrast are governed by the deformation of the membrane structure induced by hypersound. Upon turning on the hypersound, wave-like patterns were observed on the surface of the SLB (which can be observed as well by the fluorescent SLB in Videos S1–S3, ESI†), centered at the resonator and radiating outward, which indicates the propagation of hypersound within the bilayer structure. As the zoom-in image in Fig. 6a shows, the morphology of the lipid membrane was affected by the propagation of hypersound.

Subsequently, the morphology of the section of the SLB on top of the gold electrode was analyzed to evaluate the membrane structure affected by the propagation of hypersound. For comparison, the surface of the SLB was first imaged without any stimulation of hypersound (Fig. 6b), which indicates a uniform and featureless surface without defects. However, upon switching on the hypersound (500 mW, <1 min), some sub-micrometer features were immediately generated on the SLB at the same position (Fig. 6c, see zoom-in image). Although the exact sizes of the pores cannot be accurately determined because of the limitation by optical resolution of the confocal microscope, these results confirm the formation of pore structures induced by the deformation of the SLB with hypersound propagating within the membrane.

Conclusions

In this work, the behavior of a supported lipid bilayer (SLB) stimulated by hypersound of gigahertz frequency was characterized by a microchip integrating a nano-electromechanical system (NEMS) resonator and a gold electrode, which facilitates the real-time electrical detection of hypersonic poration. The ''gating''-shaped current induced by hypersound revealed that some pores were created in the SLB with the propagation of hypersound, which resembles the behavior of ion channels at lipid membranes. It was found that the formation of these pore structures was instantaneous (at least sub-second, as we did not probe the dynamics any faster) in response to hypersound, indicating that the number and/or lifetime of hypersonic pores can be controlled in a real-time manner by correspondingly adjusting the duration and input power of hypersound. The effects of ion valence and/or concentration on the formation of hypersound-induced current confirms the behavior of hypersonic nanopores in lipid membranes as the ion channel. Furthermore, characterization experiments (cyclic voltammetry, atomic force microscopy and laser scanning microscopy) showed that during the propagation of hypersound within the SLB, the membrane was laterally deformed, which supports the formation of transient pore-like defects. The generation of switchable and reversible nanopores enables the active control of membrane permeability, which can be further applied in controlled release and drug delivery systems.

Conflicts of interest

The authors declare no competing financial interest.

Acknowledgements

The authors gratefully acknowledge financial support from the National Natural Science Foundation of China (NSFC No. 61674114, 91743110, 21861132001), National Key R&D Program of China (2017YFF0204600), Tianjin Applied Basic Research and Advanced Technology (17JCJQJC43600), the Foundation for Talent Scientists of Nanchang Institute for Microtechnology of Tianjin University, the 111 Project (B07014), and the Netherlands Organization for Scientific Research (NWO; NSFC-NWO grant no. 729001032 to J. H. and X. D.).

References

1 J. Bischof, J. Padanilam, W. H. Holmes, R. Ezzell, R. Lee, R. Tompkins, M. Yarmush and M. Toner, Dynamics of cell membrane permeability changes at supraphysiological temperatures, *Biophys. J.*, 1995, **68**, 2608–2614.
2 R. H. Guy, *Transdermal drug delivery. Drug Delivery*, Springer, Berlin, Heidelberg, 2010.
3 X. He, A. A. Amin, A. Fowler and M. Toner, Thermally induced introduction of trehalose into primary rat hepatocytes, *Cell Preserv. Technol.*, 2006, **4**, 178–187.
4 J. S. Soughayer, T. Krasieva, S. C. Jacobson, J. M. Ramsey, B. J. Tromberg and N. L. Allbritton, Characterization of cellular optoporation with distance, *Anal. Chem.*, 2000, **72**, 1342–1347.
5 J. Baumgart, L. Humbert, É. Boulais, R. Lachaine, J.-J. Lebrun and M. Meunier, Off-resonance plasmonic enhanced femtosecond laser optoporation and transfection of cancer cells, *Biomaterials*, 2012, **33**, 2345–2350.
6 M. Waleed, S.-U. Hwang, J.-D. Kim, I. Shabbir, S.-M. Shin and Y.-G. Lee, Single-cell optoporation and transfection using femtosecond laser and optical tweezers, *Biomed. Opt. Express*, 2013, **4**, 1533–1547.
7 W. J. Dower, J. F. Miller and C. W. Ragsdale, High efficiency transformation of *E. coli* by high voltage electroporation, *Nucleic Acids Res.*, 1988, **16**, 6127–6145.
8 M. L. Yarmush, A. Golberg, G. Serša, T. Kotnik and D. Miklavčič, Electroporation-based technologies for medicine: principles, applications, and challenges, *Annu. Rev. Biomed. Eng.*, 2014, **16**, 295–320.
9 M. R. Prausnitz, A practical assessment of transdermal drug delivery by skin electroporation, *Adv. Drug Delivery Rev.*, 1999, **35**, 61–76.
10 R. Abdalkader, S. Kawakami, J. Unga, Y. Higuchi, R. Suzuki, K. Maruyama, F. Yamashita and M. Hashida, The development of mechanically formed stable nanobubbles intended for sonoporation-mediated gene transfection, *Drug Delivery*, 2017, **24**, 320–327.
11 S. Mehier-Humbert, T. Bettinger, F. Yan and R. H. Guy, Plasma membrane poration induced by ultrasound exposure: implication for drug delivery, *J. Controlled Release*, 2005, **104**, 213–222.
12 K. Ferrara, R. Pollard and M. Borden, Ultrasound microbubble contrast agents: fundamentals and application to gene and drug delivery, *Annu. Rev. Biomed. Eng.*, 2007, **9**, 415–447.

13 S. Mitragotri, Healing sound: the use of ultrasound in drug delivery and other therapeutic applications, *Nat. Rev. Drug Discovery*, 2005, **4**, 255–260.
14 S. Hernot and A. L. Klibanov, Microbubbles in ultrasound-triggered drug and gene delivery, *Adv. Drug Delivery Rev.*, 2008, **60**, 1153–1166.
15 K. Hynynen, Ultrasound for drug and gene delivery to the brain, *Adv. Drug Delivery Rev.*, 2008, **60**, 1209–1217.
16 T. Boissenot, A. Bordat, E. Fattal and N. Tsapis, Ultrasound-triggered drug delivery for cancer treatment using drug delivery systems: from theoretical considerations to practical applications, *J. Controlled Release*, 2016, **241**, 144–163.
17 P. Qin, L. Xu, W. Zhong and C. Alfred, Ultrasound-microbubble mediated cavitation of plant cells: effects on morphology and viability, *Ultrasound Med. Biol.*, 2012, **38**, 1085–1096.
18 C. Newman and T. Bettinger, Gene therapy progress and prospects: ultrasound for gene transfer, *Gene Ther.*, 2007, **14**, 465–475.
19 K. Kooiman, H. J. Vos, M. Versluis and N. de Jong, Acoustic behavior of microbubbles and implications for drug delivery, *Adv. Drug Delivery Rev.*, 2014, **72**, 28–48.
20 I. Lentacker, I. De Cock, R. Deckers, S. De Smedt and C. Moonen, Understanding ultrasound induced sonoporation: definitions and underlying mechanisms, *Adv. Drug Delivery Rev.*, 2014, **72**, 49–64.
21 K. S. Suslick, *Ultrasound: its chemical, physical, and biological effects*, VCH Publishers, 1988.
22 R. Pecha and B. Gompf, Microimplosions: cavitation collapse and shock wave emission on a nanosecond time scale, *Phys. Rev. Lett.*, 2000, **84**, 1328–1334.
23 G. A. Husseini, W. G. Pitt and A. M. Martins, Ultrasonically triggered drug delivery: breaking the barrier, *Colloids Surf., B*, 2014, **123**, 364–386.
24 B. Pollet, *Power ultrasound in electrochemistry: from versatile laboratory tool to engineering solution*, John Wiley & Sons, 2012.
25 Z. Izadifar, P. Babyn and D. Chapman, Mechanical and Biological Effects of Ultrasound: A Review of Present Knowledge, *Ultrasound Med. Biol.*, 2017, **43**, 1085–1104.
26 A. Van Wamel, K. Kooiman, M. Harteveld, M. Emmer, J. Folkert, M. Versluis and N. De Jong, Vibrating microbubbles poking individual cells: drug transfer into cells via sonoporation, *J. Controlled Release*, 2006, **112**, 149–155.
27 B. Lammertink, R. Deckers, G. Storm, C. Moonen and C. Bos, Duration of ultrasound-mediated enhanced plasma membrane permeability, *Int. J. Pharmaceut.*, 2015, **482**, 92–98.
28 R. Karshafian, P. D. Bevan, R. Williams, S. Samac and P. N. Burns, Sonoporation by ultrasound-activated microbubble contrast agents: effect of acoustic exposure parameters on cell membrane permeability and cell viability, *Ultrasound Med. Biol.*, 2009, **35**, 847–860.
29 K. S. Suslick, Sonochemistry, *Science*, 1990, **247**, 1439–1446.
30 B. Krasovitski, V. Frenkel, S. Shoham and E. Kimmel, Intramembrane cavitation as a unifying mechanism for ultrasound-induced bioeffects, *Proc. Natl. Acad. Sci. U. S. A.*, 2011, **108**, 3258–3263.
31 J. Wu and W. L. Nyborg, Ultrasound, cavitation bubbles and their interaction with cells, *Adv. Drug Delivery Rev.*, 2008, **60**, 1103–1116.
32 W. D. O'Brien, Ultrasound–biophysics mechanisms, *Prog. Biophys. Mol. Biol.*, 2007, **93**, 212–255.
33 S. Ramesan, A. R. Rezk and L. Y. Yeo, High frequency acoustic permeabilisation of drugs through tissue for localised mucosal delivery, *Lab Chip*, 2018, **18**, 3272–3284.
34 H. Bömmel and K. Dransfeld, Attenuation of hypersonic waves in quartz, *Phys. Rev. Lett.*, 1959, **2**, 298–305.
35 H. Bömmel and K. Dransfeld, Excitation and attenuation of hypersonic waves in quartz, *Phys. Rev.*, 1960, **117**, 1245.
36 Y. Lu, W. De Vries, N. J. Overeem, X. Duan, H. X. Zhang, H. Zhang, W. Pang, B. J. Ravoo and J. Huskens, Controlled and Tunable Loading and Release of Vesicles Using Gigahertz Acoustics, *Angew. Chem., Int. Ed.*, 2019, **58**, 159–163.
37 Z. Zhang, Y. Wang, H. Zhang, Z. Tang, W. Liu, Y. Lu, Z. Wang, H. Yang, W. Pang and H. Zhang, Hypersonic Poration: A New Versatile Cell Poration Method to Enhance Cellular Uptake Using a Piezoelectric Nano Electromechanical Device, *Small*, 2017, **13**, 1602962.
38 Z. Zhang, Z. Tang, W. Liu, H. Zhang, Y. Lu, Y. Wang, W. Pang, H. Zhang and X. Duan, Acoustically Triggered Disassembly of Multilayered Polyelectrolyte Thin Films through Gigahertz Resonators for Controlled Drug Release Applications, *Micromachines*, 2016, **7**, 194–205.
39 T. Goda and Y. Miyahara, A hairpin DNA aptamer coupled with groove binders as a smart switch for a field-effect transistor biosensor, *Biosens. Bioelectron.*, 2012, **32**, 244–249.
40 W. Guan, X. Duan and M. A. Reed, Highly specific and sensitive non-enzymatic determination of uric acid in serum and urine by extended gate field effect transistor sensors, *Biosens. Bioelectron.*, 2014, **51**, 225–231.
41 A. Ulman, *An Introduction to Ultrathin Organic Films: From Langmuir–Blodgett to Self-Assembly*, Academic press, 2013.
42 J. Liu and J. C. Conboy, Structure of a Gel Phase Lipid Bilayer Prepared by the Langmuir−Blodgett/Langmuir-Schaefer Method Characterized by Sum-Frequency Vibrational Spectroscopy, *Langmuir*, 2005, **21**, 9091–9097.
43 W. Liu, H. Zhang, H. Zhao, Z. Tang, Y. Wang, C. Sun, W. Pang and X. Duan, Comparative analysis of static and non-static assays for biochemical sensing using on-chip integrated field effect transistors and solidly mounted resonators, *Sens. Actuators, B*, 2017, **243**, 775–783.
44 R. C. Ruby, P. Bradley, Y. Oshmyansky, A. Chien and J. Larson, In Thin film bulk wave acoustic resonators (FBAR) for wireless applications, *Proc. - IEEE Ultrason. Symp.*, 2001, **1**, 813–821.
45 S.-H. Lee, K. H. Yoon and J.-K. Lee, Influence of electrode configurations on the quality factor and piezoelectric coupling constant of solidly mounted bulk acoustic wave resonators, *J. Appl. Phys.*, 2002, **92**, 4062–4069.
46 G. G. Harman, *Wire bonding in microelectronics*, McGraw-Hill, 2010.

47 W. Pang, H. Zhao, E. S. Kim, H. Zhang, H. Yu and X. Hu, Piezoelectric microelectromechanical resonant sensors for chemical and biological detection, *Lab Chip*, 2012, **12**, 29–44.

48 M. Nirschl, M. Schreiter and J. Vörös, Comparison of FBAR and QCM-D sensitivity dependence on adlayer thickness and viscosity, *Sens. Actuators, A*, 2011, **165**, 415–421.

49 G. Wiegand, N. Arribas-Layton, H. Hillebrandt, E. Sackmann and P. Wagner, Electrical properties of supported lipid bilayer membranes, *J. Phys. Chem. B*, 2002, **106**, 4245–4254.

50 S. Pan, H. Zhang, W. Liu, Y. Wang, W. Pang and X. Duan, Biofouling Removal and Protein Detection Using a Hypersonic Resonator, *ACS Sens.*, 2017, **2**, 1175–1183.

51 H. Bayley and P. S. Cremer, Stochastic sensors inspired by biology, *Nature*, 2001, **413**, 226–230.

52 M. A. IUPAC and A. Wilkinson, *IUPAC Compendium of Chemical Terminology: the Gold Book*, Oxford, 1997.

53 J. D. Unsay, K. Cosentino and A. J. García-Sáez, Atomic force microscopy imaging and force spectroscopy of supported lipid bilayers, *J. Visualized Exp.*, 2015, **101**, 52867–52875.

